Inorganic Chemistry

Article

pubs.acs.org/IC

Supramolecular Anchoring of Octahedral Molybdenum Clusters onto Graphene and Their Synergies in Photocatalytic Water Reduction

Marta Feliz,*[,†] Pedro Atienzar,[†] Maria Amela-Cortés,[‡] Noée Dumait,[‡] Pierric Lemoine,[‡] Yann Molard,*[,‡] and Stéphane Cordier[‡]

[†]Instituto de Tecnología Química, Universitat Politècnica de València, Consejo Superior de Investigaciones Científicas Avenida de los Naranjos s/n, 46022 Valencia, Spain

[‡]Université de Rennes, CNRS, ISCR-UMR 6226, ScanMAT-UMS 2001, F-35000 Rennes, France

Supporting Information

ABSTRACT: Dihydrogen (H_2) production from sunlight should become one of the most important energy production means in the future. To reach this goal, low-cost and efficient photocatalysts still need to be discovered. Here we show that red near-IR luminescent metal cluster anions, once combined with pyrene-containing cations, are able to photocatalytically produce molecular hydrogen from water. The pyrene moieties act simultaneously as energy transmitters and as supramolecular linkers between the cluster anions and graphene. This association results in a hybrid material combining the emission abilities of pyrene and cluster moieties with the electronic conduction efficiency of graphene. Hydrogen evolution reaction (HER) studies show that this association induces a significant increase of H_2 production compared to that produced separately by clusters or graphene. Considering the versatility of the strategy described to design this photocatalytic hybrid material, transition-metal clusters are promising candidates to develop new, environmentally friendly, and low-cost photocatalysts for HER.

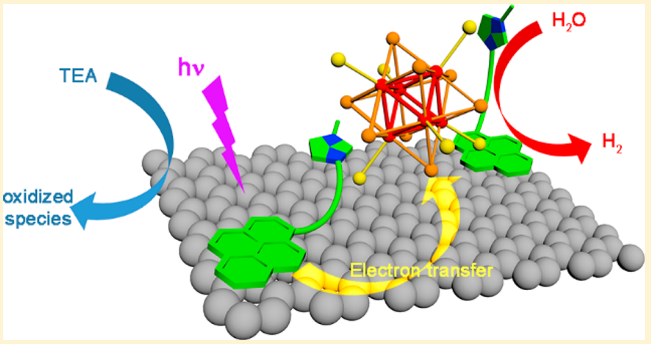

INTRODUCTION

Transition-metal clusters are molecular compounds that contain several metal atoms linked by metal−metal bonds.[1] With their exact and defined composition, they can be classified as intermediates between transition-metal coordination complexes and metal nanoparticles. Their specificity, compared to coordination complexes, is the delocalization of electrons involved in the metal−metal bonds on the whole metallic architecture. Because those are not confined on one metal center, transition-metal clusters display intermediate behavior between atoms and bulk metals and, in particular, show unique magnetic, optical, or catalytic properties.[2−10] Yet, octahedral transition-metal cluster compounds based on a molybdenum, tungsten, or rhenium scaffold (Scheme 1a) are particularly attractive in the design of functional hybrid nanomaterials with potential applications in optoelectronic,[11−16] lighting,[17] theranostic,[18−21] or photocatalysis[6,7,9,22] applications. Because molybdenum or tungsten elements are cheap and abundant, cluster-based compounds constitute promising alternatives to costly iridium(III)-, platinum(II)-, or rare-earth-containing luminophores or nonenvironmentally friendly lead hybrid perovskites or cadmium-containing quantum dots. They are synthesized as $A_x[M_6X^i_8X^a_6]$ ternary alkali salts (A = alkali, x = 2−4; X^i = inner ligand, usually halogen or chalcogen atoms; X^a = apical halogen ligand) using solid-state chemistry techniques. The resulting powders or crystals behave like ceramics. That is probably the reason why, despite their outstanding functionalities, their use and studies were circumvented to a small community of scientists who, only around 20 years ago, opened Pandora's box of their integration into functional materials and nanocomposites[23,24] via solution chemistry. Because octahedral transition-metal clusters form an integral part of nanoscience and were integrated into functional hybrid materials by various approaches by either direct integration or, after apical ligand exchange, cationic metathesis or host−guest complexation.[25−28] Among the metal cluster units, the $[M_6I^i_8(perfluoroalkylate)^a_6]^{2-}$ and $[M_6I^i_8(perfluorobenzoate)^a_6]^{2-}$ (M = Mo, W) cluster anions are the most emissive, with emission properties depending on the pK_a values of the carboxylic acids.[29−36] Recently, they were used to develop theranostic tools,[37] lighting devices,[17] or oxygen sensors,[38] but, surprisingly, their catalytic abilities have been scarcely explored so far. Yet, their excellent abilities to emit light combined with their isotropic architecture, i.e., the presence of six metal atoms

Received: August 21, 2019

DOI: 10.1021/acs.inorgchem.9b02529
Inorg. Chem. XXXX, XXX, XXX−XXX

Scheme 1. Schematic Representation of the Cluster Compound Precursor and Organic Imidazolium Salts Synthesized for These Studies (a) and the Hybrids Py_2Mo and Im_2Mo That Will Be Further Grafted onto Graphene Surfaces (b)

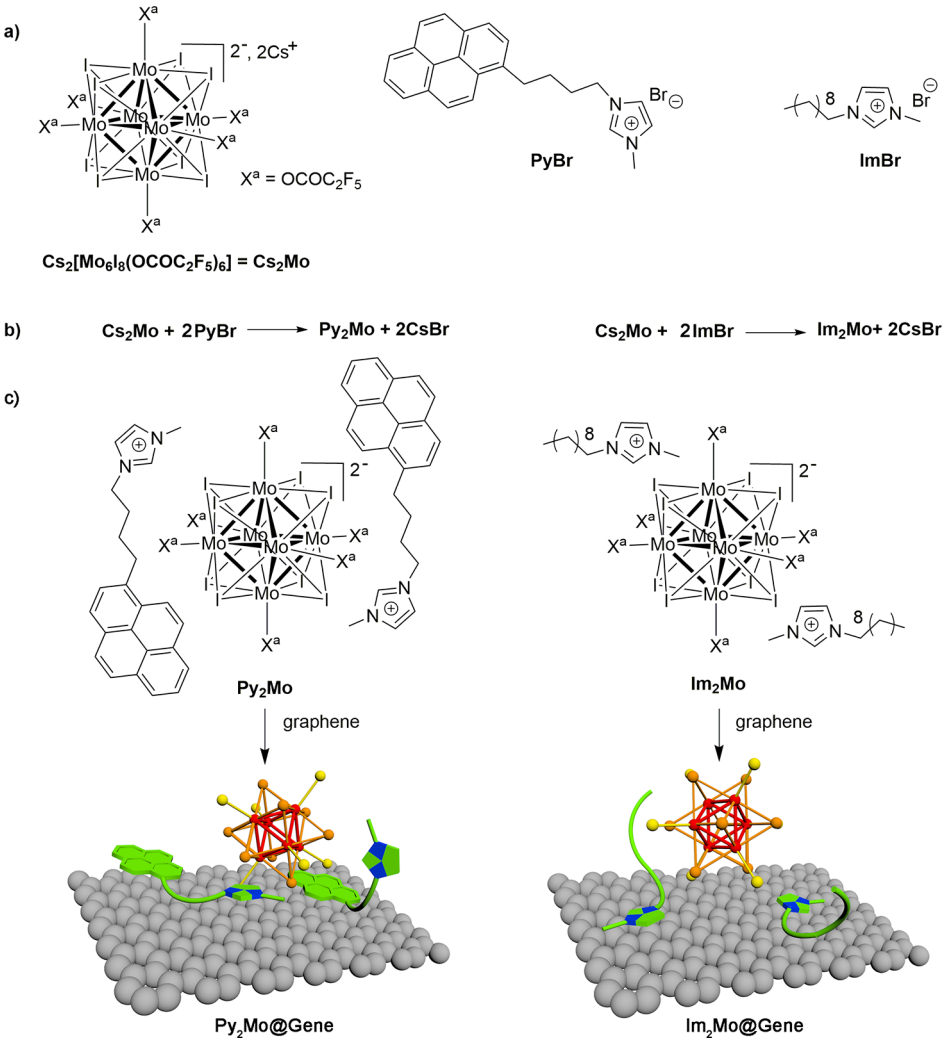

arranged orthogonally, which could all play the role of catalytic center, prefigure good opportunities in photocatalysis for this family of compounds. In this work, we investigate the photocatalytic abilities of a $[Mo_6I^i_8(OCOC_2F_5)^a_6]^{2-}$ anion,[33] in one of the most emblematic reactions in the field of renewable energy: the production of hydrogen by water splitting using sunlight.[39−42] In this field, it is still very challenging to develop low-cost, but efficient enough, photocatalysts that can be further scaled up for industrial applications.[39,42−52] Currently, most researches are directed toward the use of earth-abundant transition-metal materials and hybrid systems supported on graphene.[42,53−58] The potential of transition-metal complex-based photocatalysts to replace conventional inorganic materials was recently reported.[59] Still, many challenges should be faced before graphene-metal cluster nanocomposites become photocatalysts to address environmental and energy-related issues, for instance, in terms of the photostability and activity.[60,61] In fact, it is well-known that graphene, because of its zero-band-gap semiconducting properties due to its extended conjugated system, possesses a high conductivity and electron mobility that favor charge separation and electron transport. Therefore, supporting photocatalysts on graphene usually prevents the direct recombination of the hole−electron pair formed during light excitation and, as a result, facilitates photogenerated electron transfer, leading to an enhanced H_2 photocatalytic performance compared to neat photocatalysts. Hence, several photocatalysts, such as TiO_2 nanoparticles, CdQ (Q = S, Se) quantum dots, MoS_2, or, more recently, metal clusters, were supported on graphene oxide (GO) or reduced graphene oxide (RGO).[42,62−66]

Here we report on the synthesis, characterization, and photophysical properties of bright-red near-IR (NIR)-emitting octahedral molybdenum cluster complexes bearing functional organic countercations able to form a supramolecular adduct with graphene. The properties of the most promising candidate in terms of surface coverage were further investigated, in particular the photocatalytic efficiency in the hydrogen evolution reaction (HER) from water.

RESULTS AND DISCUSSION

Designing the Linker for the Anchoring of a Transition-Metal Cluster on the Graphene Sheet: The Supramolecular Way. It is now recognized that $[M_6X^i_8X^a_6]^{2-}$ emission properties are related to the pK_a value of their apical ligands and that the most efficient emitters possess apical ligands linked to metal atoms via an acetate function.[30,34,36] Hence, the integrity of the

DOI: 10.1021/acs.inorgchem.9b02529
Inorg. Chem. XXXX, XXX, XXX−XXX

$[Mo_6I^i_8(OCOC_2F_5)^a_6]^{2-}$ anion should be preserved within the photocatalytic system to preserve its outstanding ability to emit light. In earlier studies, we observed that the covalent grafting of metal clusters on the surface of GO sheets limited accessibility to the cluster active sites for catalytic reactions.[9] Moreover, the graphene covalent functionalization alters the sp^2 structure of its lattice, which results in defects and a loss of electronic properties. Therefore, the apical ligand-exchange approach, which allows the covalent grafting of the polymetallic anion onto any type of surface,[67−69] has to be discarded. The noncovalent functionalization of graphene preserves its outstanding structural and electronic properties along with the simultaneous deposition of new chemical groups on the surface and leads to enhanced dispersibility and catalytic reactivity of the hybrid material. For these reasons, using noncovalent interactions to link both protagonists appears to be the most profitable way to take advantage of their properties. In fact, noncovalent functionalization of graphene or GO has been extensively studied to bind fluorophores or functional organic or inorganic species onto their surface.[65,70−72] This technique should lead to hybrid materials that combine the best of each of the individual component properties. Hence, using supramolecular interactions to maintain the cluster anion on the graphene surface seems to be the more appropriate method to maximize the cluster effect during catalytic reactions.

The adsorption of polycyclic aromatic hydrocarbons and ionic liquids based on imidazolium cations onto graphene nanosheets has recently been investigated.[73,74] In the case of pyrene, its affinity to graphene is dominated by $\pi-\pi$ interactions, whereas in the case of ionic liquids, these and other noncovalent interactions, such as C−H···π, N···π, or ion···π interactions, take place in the adsorption of imidazolium cations and their associated counteranions on the graphene surface.[74,75] Recently, Coskun and co-workers have shown that bifunctional pyrene−imidazolium molecules can interact with RGO through $\pi-\pi$ and cation−π interactions simultaneously with ionic liquid solvent molecules.[76] In this context, as depicted in Scheme 1a, we decided to synthesize an imidazolium cation bearing a pyrene group, noted as **Py**$^+$ (1-methyl-3-[4-(pyren-1-yl)butyl]-1*H*-imidazol-3-ium), to counter the anionic charge of the metal cluster unit. Photoactive cluster units bearing planar aromatic molecules can add light-harvesting,[77] energy-transfer (ET), and charge-transfer features to graphene. The *N*-methylimidazolium-funtionalized pyrene counterions should play a dual role: (i) to act as antenna and promote ET to the luminescent $\{Mo_6I^i_8\}^{4+}$ cluster core and (ii) to assist cluster immobilization on graphene surfaces by noncovalent interactions. To observe the benefit of the pyrene group on its functional ability to be adsorbed on the graphene surface, we also functionalized the cluster anion with imidazolium cations bearing a long alkyl chain, noted as **Im**$^+$ (1-methyl-3-nonyl-1*H*-imidazol-3-ium).

Synthesis and Characterization of the Py_2Mo, Im_2Mo, and Py_2Mo@Gene Materials. The cationic metathesis between the $Cs_2[Mo_6I^i_8(OCOC_2F_5)^a_6]$ (**Cs_2Mo**) compound and the **PyBr** or **ImBr** salts affords quantitatively the **Py_2Mo** and **Im_2Mo** complexes, respectively, as highlighted in Scheme 1b. The **Py_2Mo** and **Im_2Mo** cluster compounds were characterized by ^{1}H and ^{19}F NMR spectroscopy, and electrospray ionization mass spectrometry (ESI-MS) in order to confirm the complexes' identity and purity (see the Experimental Section and Supporting Information for characterization details). The structure of the **Py_2Mo** complex was further confirmed by single-crystal X-ray diffraction (XRD) on suitable crystals obtained by the slow evaporation of a complex containing an acetone/toluene (1:1) solution (see the Supporting Information).

The adsorption capacities of **Py_2Mo** and **Im_2Mo** by noncovalent interactions on the graphene surface, resulting in **Py_2Mo@Gene** and **Im_2Mo@Gene** hybrid nanomaterials, respectively (Scheme 1c), were investigated. The corresponding adsorption densities (q_e) and adsorption isotherms were also determined (Figure S3). The maximum adsorption capacity observed for **Py_2Mo** at equilibrium is 0.3827 mmol of **Py_2Mo**/g of graphene. Considering the surface area of graphene (474 m^2/g), the calculated cluster density deposited on the graphene surface is 0.0008 mmol/m^2. The maximum q_e determined for **Py_2Mo** is less than that reported for pyrene,[74] which is probably due to the high steric hindrance of the hybrid complex and the fact that two pyrene moieties are surrounding one metal cluster unit. The adsorption isotherms for both complexes show a linear fitting, in agreement with the Langmuir isotherms, with ca. 15% increment of the adsorption capacities for **Py_2Mo** versus **Im_2Mo**. These results support the relevant role of pyrene in reinforcing noncovalent cluster immobilization on the graphene surfaces despite its bulkiness compared to the **Im**$^+$ cation. Hence, because the pyrene-containing cation is the one that provides the best surface coverage, only the hybrid cluster compound **Py_2Mo** and its adduct with graphene were further investigated. **Py_2Mo@Gene** was thus obtained by mixing **Py_2Mo** and graphene in dichloromethane at room temperature. The solid nanomaterial was isolated by filtration and washed with dichloromethane and diethyl ether, followed by vacuum drying.

The morphology of the **Py_2Mo@Gene** material was characterized by high-resolution transmission electron microscopy (HR-TEM). HR-TEM analyses of the **Py_2Mo@Gene** material shows a heterogeneous distribution of 2−3 nm molybdenum cluster aggregates onto a few-layer graphene support (Figure S4). The $\pi-\pi$ and cation−π interactions between the pyrene-functionalized imidazolium cations and graphene allow the hybrid system to self-assemble strongly, and these interactions also lead to the entrapment of cluster molecules between graphene layers, resulting in the formation of a 3D network structure. In addition, the cluster anion−π interactions are not discarded in the adsorptive interactions.[75] The energy-dispersive X-ray spectroscopy and scanning transmission electron microscopy (EDS/STEM) analysis of the hybrid material confirms the presence of molybdenum, iodine, and fluorine atoms (Figure S5).

The **Py_2Mo@Gene** nanomaterial was further characterized by Fourier transform infrared (FT-IR), Raman, and photophysical-based techniques. The IR spectra registered for the **Py_2Mo@Gene**, **Py_2Mo**, and graphene materials (Figure 1a) shows that there is no shift of the **Py_2Mo** and graphene peaks after cluster immobilization. The IR spectrum of the **Py_2Mo@Gene** solid contains most of the characteristic peaks of the **Py_2Mo** complex. The bands at 1580 and 1628 cm^{-1} of the graphenic materials are assigned to the C=C vibrations of the sp^2 carbon atoms and H−O−H vibrations of adsorbed water molecules, respectively. The Raman spectra of **Py_2Mo**, graphene, and the hybrid nanomaterial have been acquired in the solid state upon 325 nm laser irradiation (Figure 1b). The Raman bands between 150 and 500 cm^{-1} expected for the $\{Mo_6X^i_8\}^{4+}$ (X = halogen) cluster core complexes are not

DOI: 10.1021/acs.inorgchem.9b02529
Inorg. Chem. XXXX, XXX, XXX−XXX

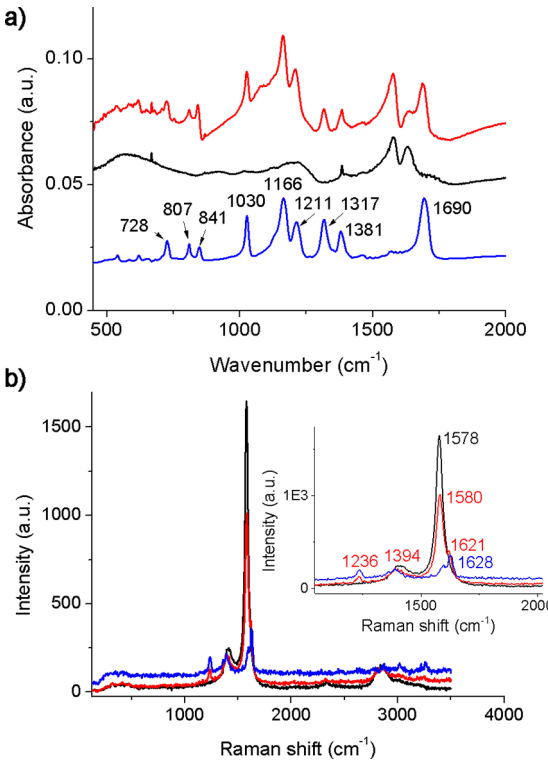

Figure 1. (a) FT-IR (KBr) spectra of **Py_2Mo@Gene** (red line), **Py_2Mo** (blue line), and graphene (black line). The **Py_2Mo** and graphene bands are highlighted. b) Raman spectra of **Py_2Mo@Gene** (red line), **Py_2Mo** (blue line), and graphene (black line). The inset shows the characteristic pyrene and graphene bands.

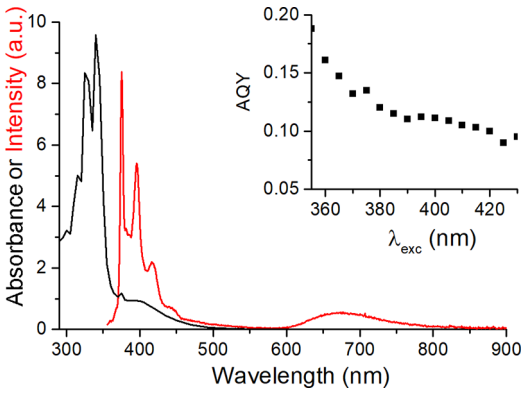

Figure 2. Absorption (black line) and emission (red line) spectra of **Py_2Mo** in a deaerated solution (λ_{exc} = 345 nm). Inset: AQY versus excitation wavelength.

detectable, and only fluorescence has been obtained under 514 and 785 nm laser conditions.[78,79] The **Py_2Mo@Gene** spectrum contains a very intense band at 1580 cm^{-1} (G band) characteristic of the graphene aromatic rings−sp^2 carbon atoms vibration.[80] A wide band with a lower intensity appears at 1394 cm^{-1} and includes a pyrene group Raman shift and the D band of graphene support. Two additional low-intensity bands characteristic of the pyrene functionality appear at 1236 and 1621 cm^{-1}.[81,82] The graphenic 2D band (2848 cm^{-1}) does not show any displacement after cluster immobilization.

Photophysical Properties of the Py_2Mo and Py_2Mo@Gene Materials. The photophysical properties of **Py_2Mo** were investigated in solution and compared to those of the **PyBr** and **Cs_2Mo** precursors. The **Py_2Mo** absorption spectrum shows the strongly pyrene-absorbing bands centered at 325 nm (Figure 2) associated with the $S_0 \rightarrow S_2$ transition, by analogy with similar systems.[82−84] The low absorption band intensity at 403 nm is associated with a metal-to-metal charge-transfer (^{1}MMCT) transition within the $\{Mo_6I^i_8\}^{4+}$ cluster core.[85,86] This band is also observed in the **Cs_2Mo** compound (Figure S6), which also shows absorption bands centered at 334 and 295 nm characteristic of the molybdenum-to-ligand cluster transitions. The appearance of these UV bands implies that there is a cluster contribution in the pyrene absorption region of the **Py_2Mo** cluster compound (see the **PyBr** absorption spectrum in Figure S6 for a comparison). The emission spectrum of **Py_2Mo** in deaerated solution is presented in Figure 2. Upon excitation (λ_{exc} = 310−375 nm), two emission bands appear in the red and blue regions of the spectrum. The vibrational structure of the pyrene observed in the steady-state fluorescence spectrum appears to be a mirror image of the absorption spectrum. This fluorescence takes place from the S_1 state and is due to a rapid internal conversion from the S_2 state to the S_1 state upon excitation into the most intense pyrene absorption band centered at 345 nm.[87] Despite the presence of two pyrene units per **Py_2Mo**, the excimer emission from pyrene at ca. 500 nm is not observed. This highlights the lack of intra- and intermolecular pyrene−pyrene interactions, taking into consideration the high dilution conditions (10^{-5}−10^{-6} M). A low-intensity band with a maximum localized at 675 nm, attributed to the molybdenum cluster core emission, is also detected. This emission band shows a bathochromic shift with respect to the emission wavelength (650 nm) measured in *N*,*N*-dimethylformamide (DMF), also reported for **Cs_2Mo** in the solid state.[33] The disappearance of this band by bubbling O_2 into the **Py_2Mo**-containing solution confirms the oxygen quenching of the cluster unit phosphorescence. The absolute quantum yield (AQY) of **Py_2Mo** was measured exciting the sample every 5 nm from 355 up to 430 nm. The AQY decreases from 0.18 to 0.12, and from 355 to 380 nm is when the pyrene emission is visible. This value stabilizes around 0.1 when the cluster is the only emitter. The $\{Mo_6I^i_8\}^{4+}$ cluster core bearing perfluoroalkylcarboxylates presents one of the highest quantum yield values among the octahedral $\{M_6X^i_8\}^{4+}$ (M = Mo, W, Re; L^i = halogen, chalcogen) cluster complexes, and quantum yields of 1 and 0.59 in solution were reported for $(nBu_4N)_2[Mo_6I_8(OOCCF_3)_6]$ and $(nBu_4N)_2[Mo_6I_8(OOCC_3F_7)_6]$, respectively,[30,31] while we recently reported an AQY value of 0.49 in deaerated acetone for **Cs_2Mo**.[17] Therefore, the **Py_2Mo** AQY value is lower than that calculated for its precursor **Cs_2Mo**. In a first attempt, this observation can be explained as follows: the metal cluster red emission at 675 nm is subject to a partial ET mechanism associated with intermolecular interactions between the pyrene and molybdenum cluster. This ET is partly due to the spectral overlap between the emission band of the pyrene moiety and the absorption band of the molybdenum cluster. A triplet−triplet state equilibrium between the triplet state of pyrene and that of the cluster could then be envisioned. This equilibrium would favor nonradiative relaxation of the excited states (vide infra). Figure 3 presents the evolution of the emission intensity maximum value of both entities versus excitation wavelength from 310 nm up to 390 nm and the excitation map for excitations ranging from 355 up to 500 nm. The optimal wavelength to observe the pyrene emission is, as expected, around its maximum of absorption. Meanwhile, a band

DOI: 10.1021/acs.inorgchem.9b02529
Inorg. Chem. XXXX, XXX, XXX−XXX

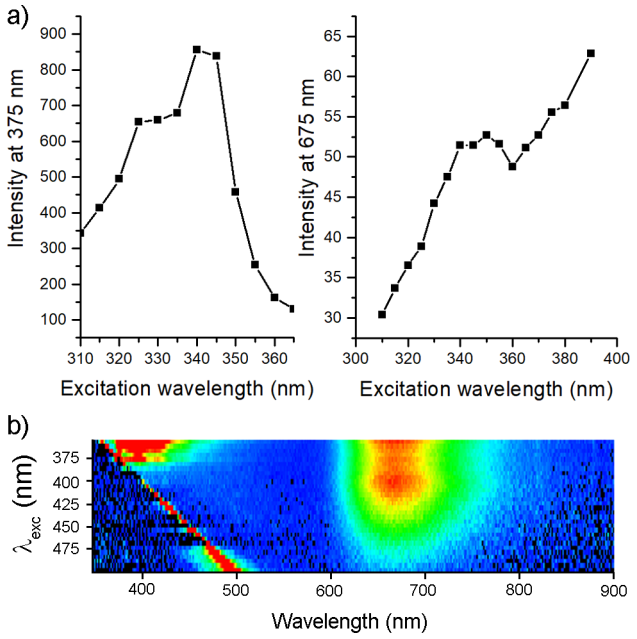

Figure 3. (a) Evolution of **Py_2Mo** emission maxima at 375 and 675 nm upon excitation. (b) Emission versus excitation map of **Py_2Mo** (the emission intensity increases from dark blue to red).

followed by a slight intensity decrease can be observed between 340 and 360 nm for the molybdenum cluster, in agreement with the maximum absorption of the pyrene group. This disruption in the emission evolution trend is followed by an increase when the cluster is the only species to absorb (see Figure S7 for the corresponding emission spectra). Then, the cluster emission slowly decreases because of its absorption lowering up to 500 nm. To assess in a first attempt that an effective transfer exists between the pyrene moieties and anionic cluster unit, emission spectra of solutions containing **Py_2Mo** or **Cs_2Mo** at the same concentration were recorded upon a 345 nm excitation. The increase of the cluster emission intensity by approximately 30% is in good accordance with the pyrene-to-molybdenum cluster ET (Figure S8). The presence of pyrene emission signals indicates that ET from the pyrene-containing cation to the cluster core is not quantitative. Such nonquantitative ET was also recently evidenced in a solution for assemblies gathering blue-emissive triphenylene-containing imidazolium cations and red-NIR-emissive $[Re_6Se_8CN_6]^{4-}$ anions.[88] This shows that a short and covalent link between the pyrene and cluster unit is mandatory to observe a full ET between the two entities and thus enhancement of its emission efficiency.[77] We also monitored the emission signal of a solution containing initially **Cs_2Mo**, to which a small aliquot of a **PyBr** solution was added (see Figure S9 for the emission spectra). We observed an increase of the molybdenum cluster complex red emission in the presence of **PyBr**. The rise of the emission of **Cs_2Mo** in the presence of **PyBr** is again in favor of a pyrene-to-cluster ET. To further characterize this partial ET, time-dependent emission and absorption properties were investigated by time-correlated luminescence spectroscopy and transient absorption (TA) spectroscopy.

Time-resolved luminescence was also acquired at different excitation wavelengths. Emission lifetimes were extracted by fitting the experimental emission decay curves. The goodness of fits were judged by looking at the χ^2 value and shape of the residual distribution. The phosphorescence lifetime for **Py_2Mo** (188 μs, λ_{exc} = 345 nm in DMF) corresponds to the lifetime of the emissive $\{Mo_6I^i_8\}$-localized triplet states and is similar to those reported for other carboxylate $[Mo_6I^i_8(OOC\text{-}R)_6]^{2-}$ (R = CF_3, 182 μs; R = n-C_3F_7, 303 μs) complexes in acetonitrile.[30,31] The higher emission lifetime of **Cs_2Mo** (228 μs, λ_{exc} = 345 nm) suggests that the emission decay is faster for the **Py_2Mo** complex, associated with any kind of counterion−cluster interaction.[89] This decrease in the lifetime and the slight bathochromic shift of the cluster emission maximum when Cs^+ is replaced by Py^+ could be due to electronic stabilization of the cluster excited state by the pyrene−imidazolium counterion.[90−92] The decrease of the pyrene fluorescence lifetime from **PyBr** to **Py_2Mo** (200 and 164 ns, respectively, with λ_{exc} = 340 nm; see Figure S10 for the fluorescence decay profiles) confirms this partial interaction.

The TA spectra of the **PyBr** and **Py_2Mo** compounds are presented inFigure 4a. For **PyBr**, the spectrum shows the

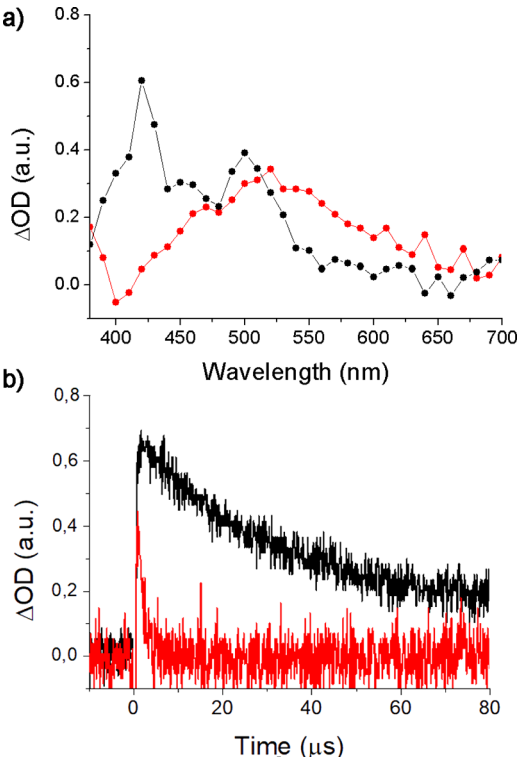

Figure 4. (a) TA (5 μs after pulse) and (b) temporal profiles of **Py_2Mo** (red) and **PyBr** (black) acquired under argon in DMF.

characteristic TAs of the pyrene-group triplet states of the functionalized imidazolium cation, which appear as two maxima centered at ca. 420 and 500 nm.[93] These triplet states are confirmed by quenching experiments with O_2 (Figure S11). At low absorption times, a negative band corresponding to the emission of the pyrene-group singlet state (Figure S12a,c) appears between 350 and 450 nm. The **Py_2Mo** and **Cs_2Mo** TA spectra acquired upon 355 nm excitation are very similar and show a broad absorption band with one maximum centered at ca. 520 and 550 nm, respectively (see Figure S12 for the TA spectrum of **Cs_2Mo**).

The temporal profiles acquired at 550 nm (Figure S13) show that the absorption lifetime of the triplet state for **Py_2Mo** is faster than that for **Cs_2Mo**, in agreement with the different lifetimes stated above. Both absorptions are sensitive to O_2,

DOI: 10.1021/acs.inorgchem.9b02529
Inorg. Chem. XXXX, XXX, XXX−XXX

indicating their triplet-state nature, as previously shown by steady-state luminescence experiments (Figure S11b,d).

The absorption temporal profiles measured for **PyBr** and **Py_2Mo** indicate that the pyrene-group triplet-state absorption at 420 nm involves a fast decay in the **Py_2Mo** compound, in contrast to the profile measured for **PyBr** (Figure 4b). This result confirms ET from the pyrene group of the imidazolium-functionalized cation excited state to the molybdenum cluster anion. Deactivation of the pyrene-group triplet state by the cluster core was confirmed by monitoring the decrease of the pyrene-group triplet state (420 nm) with the sequential addition of small volumes of a stock solution of **Cs_2Mo** to a solution of **PyBr** (see Figure S15 for temporal profiles). We propose two possible reaction paths in the ET mechanism within the **Py_2Mo** complex, by taking the energy positioning of cluster orbitals, calculated from the absorption and redox data of $[Mo_6I^i_8(OCOC_2F_5)^a_6]^{2-}$ (see section IV for details about calculations) and the pyrene orbitals.[34,94−96] In both paths, the increase of the cluster unit phosphorescence at 675 nm could be attributed to a combination of ET and intersystem crossing (ISC) processes, ensuring that the energy migrates from the pyrene group and the $\{Mo_6I^i_8\}^{4+}$-cluster-core-localized singlet excited states to the ^{3}MMCT state of the cluster unit. Upon excitation in the UV region, regarding the first mechanism proposed (blue line, Scheme 2), the pyrene group S_1 excited state transfers the absorbed energy to the molybdenum cluster S_1 excited state, and the remaining energy is lost by fluorescence relaxation. The S_1 cluster state goes forward to an ISC to the T_1 state of the $\{Mo_6I^i_8\}^{4+}$ cluster core. In a second mechanism (red line, Scheme 2), the excited state of the pyrene group of the imidazolium-functionalized counterion evolves to an ISC to its T_1 triplet state, which transfers some energy to the emissive cluster-localized triplet state. We consider that the contribution of the reaction path referring to the S_1(Py)-to-T_1(Py) ISC transition in the global mechanism is minor because of the low amount of pyrene-group triplet state formed. Thus, the preferred path corresponds to the S_1(Py)-to-S_1(Mo_6) ET transition, in agreement with previous studies realized on the $[Mo_6I^i_8(OCO\text{-pyrene})^a_6]^{2-}$ complex for which an intramolecular ET takes place quantitatively.[66] Additionally, taking into account the energy positions of T_1(Py) (−3.1 eV) and T_1(Mo_6) (−3.4 eV) as well as the low lifetime detected by TA, a triplet−triplet equilibrium can be discarded. Therefore, the reaction path referring to the S_1(Py)-to-T_1(Py) ISC transition can be considered to be less probable because of the low amount of pyrene-group triplet-state formation.

Scheme 2. Energy Diagram of the Possible Reaction Paths Based on the Photophysical Properties of Py_2Mo (ET = Energy Transfer; ISC = Intersystem Crossing)[a]

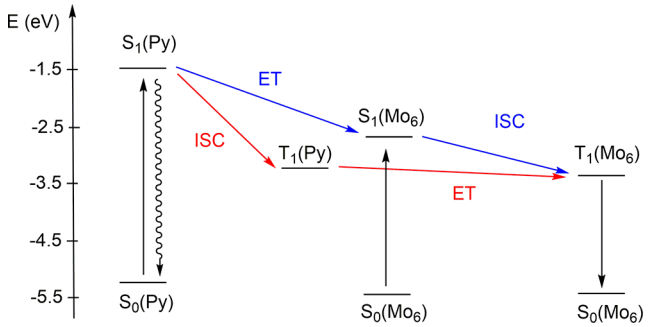

[a]Energy scale relative to a vacuum.

Interactions between Py_2Mo and Graphene in Py_2Mo@GeneS. The electronic interactions between **Py_2Mo** and graphene were evidenced by steady-state and time-resolved photoluminescence spectroscopies. In the steady-state regime, adding aliquots of a single- and few-layer-thickness graphene suspension in DMF to a DMF solution containing the **Py_2Mo** complex (λ_{exc} = 375 nm) leads to a progressive decrease of the pyrene and $\{Mo_6I^i_8\}^{4+}$ cluster core emission bands (see Figure S15a for emission spectra). This quenching of the **Py_2Mo** photoluminescence characterizes a nonradiative ET from **Py_2Mo** to the adjacent graphene surface, although photoluminescence of the graphene layers is negligible.[97] The time-resolved luminescence spectra (Figure S15b) confirm ET from the pyrene-localized excited states to the π system of graphene because the pyrene-group lifetime decreases with increasing graphene concentration. The emission decay profiles could be fitted with a double-exponential function, which indicates dynamic quenching of the pyrene-group excited states. Two lifetime components appear for each decay curve: one in the scale of the pyrene lifetime and a faster one associated with the presence of graphene. The relative ponderation of both components evolves upon the addition of graphene. In fact, the weight of the pyrene component changes from 32% after the addition of 125 μL of graphene to 14% with 850 μL of graphene suspension. These observations are also consistent with ET from **Py_2Mo** to graphene.[98] Moreover, steady-state and lifetime fluorescence quenching studies with graphene revealed deviation from linearity in the Stern−Volmer plots (Figure S16), indicating a collective effect of static and dynamic quenching. This could be explained considering the initial complex formation between the pyrene derivative compound and the graphene layers at the ground state, together with the collisional quenching of the remaining excited states of the pyrene units. The interaction between the **Py_2Mo** complex and the graphene support in the **Py_2Mo@Gene** nanomaterial was also studied by TA. The absorption spectrum of the hybrid material (Figure S17) is dominated by a broad-band absorption characteristic of graphene, which is attributed to the formation of delocalized electron and hole pairs along the nanostructure.[99,100] The TA of the **Py_2Mo@Gene** hybrid exhibits the pyrene emission band with a maximum at 400 nm and a small absorption band at 540 nm assigned to the triplet state of the molybdenum cluster. The low intensity of the molybdenum band and the short lifetimes (Figure 5)

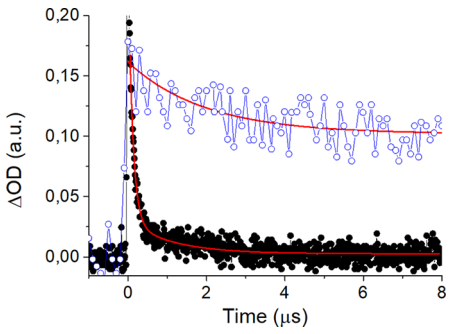

Figure 5. Absorption temporal profiles of **Py_2Mo@Gene** (0.5 mg/mL, black line) and **Py_2Mo** (blue line) monitored at 580 nm after 355 nm laser excitation of a N_2-purged dichloromethane solution.

DOI: 10.1021/acs.inorgchem.9b02529
Inorg. Chem. XXXX, XXX, XXX−XXX

associated with the temporal profiles of the **Py_2Mo@Gene** material confirm the quenching of the excited state of the molybdenum cluster by the graphene support, and suggest that any ET takes place also from the cluster complex to the graphene support.[98] Therefore, this photoinduced charge transfer from the **Py_2Mo** complex to the graphene layer produces a synergetic effect, favoring the charge-separation process after irradiation and enhancing the photocatalytic conversion as we describe below.

Photocatalytic HER Studies. A comparative photocatalytic activity study of the **Py_2Mo@Gene**, **Py_2Mo** and graphene materials for molecular hydrogen generation from water was performed in a water/acetone (50:45, v/v) mixture in the presence of triethylamine (TEA; 5% v/v) under UV−vis irradiation. Irradiations were carried out, with continuous stirring, using a cylindrical Pyrex reactor and a fiber-optic xenon light source (800−200 nm emission output, 1000 W/m^2). The evolution of photoreactions was monitored over time by means of gas chromatography. After 6 h of irradiation, dihydrogen (H_2) was the only gas generated, and the performance of the catalysts was evaluated in terms of H_2 yield. The H_2 yields (μmol of H_2/g of catalysts) with respect to time using the three photocatalysts are illustrated in Figure 6.

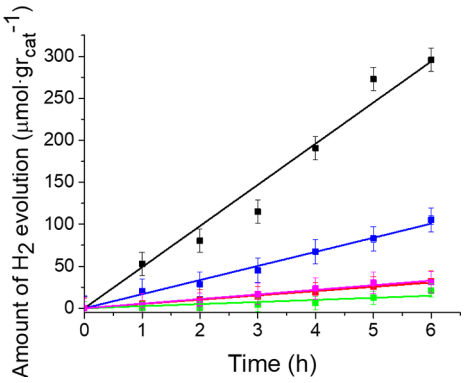

Figure 6. HER (μmol of H_2/g of catalysts) versus time plot by using **Py_2Mo@Gene** (black line), **Py_2Mo** (blue line), **PyBr** (green line), **PyBr/Gene** (pink line) and graphene (red line) catalysts. **Py_2Mo**, **PyBr**, and **PyBr/Gene** were used in amounts equal to that of **Py_2Mo@Gene**.

The nanosized **Py_2Mo@Gene** composite exhibits higher H_2 production in the photocatalytic reaction than the **Py_2Mo** and graphene counterparts, resulting in an increase of the photocatalytic activities by 280%. After 6 h of irradiation, the hydrogen formation rates by using **Py_2Mo@Gene**, **Py_2Mo**, and graphene catalysts were 49, 18, and 5 μmol of H_2/g of catalysts/h, respectively. The reaction rate of the hybrid nanomaterial is in the range of that reported for other MoS_2/graphene catalytic systems in photochemical conditions (Table S3), although other complex systems are more efficient.[101−104] The catalytic activity of **Py_2Mo@Gene** is comparable to that reported for some TiO_2-, CdS-, and C_3N_4/graphene nanomaterials in the absence of platinum as the cocatalyst.

The small amount of hydrogen generated by neat graphene can be ascribed to the production of active catalytic species by aging the graphene materials under photochemical conditions.[105] The turnover numbers calculated with respect to the **Py_2Mo** cluster for the **Py_2Mo@Gene** and **Py_2Mo** samples were found to be 0.96 and 0.34, respectively. The turnover frequency (TOF) with respect to atomic molybdenum for **Py_2Mo@Gene** corresponds to 7×10^{-6} s^{-1}. This is of the same order of magnitude as the TOF values that we observed for the $(TBA)_2Mo_6Br^i_8$@GO composite for photocatalytic HER in similar conditions, whereas the TOF for **Py_2Mo** (3×10^{-6} h^{-1}) is 2 orders of magnitude lower than that reported for the $(TBA)_2Mo_6Br^i_8F^a_6$ complex.[9] The reaction rates for the **Py_2Mo@Gene** nanomaterial and **Py_2Mo** complex are nearly constant, and no induction period appears, in contrast to the $(TBA)_2Mo_6Br^i_8F^a_6$ catalyst. This suggests that the integrity of the **Py_2Mo** species is maintained under reaction conditions. After three reuse experiments of **Py_2Mo@Gene**, the morphology of the nanomaterial remains intact (Figure S18), with 10% (w/w) molybdenum leaching after each experiment. Control experiments were carried out and show that **Im_2Mo/Gene**, **Cs_2Mo/Gene**, and **PyBr/Gene** composites are less active than the **Py_2Mo@Gene** hybrid and that H_2 production is attributed to the molybdenum clusters (Figures 6 and S24). We detect a slight increase of the activity of **Im_2Mo/Gene** with respect to **Cs_2Mo/Gene** (Figure S24), which could be attributed to a better contact of **Im_2Mo** to the graphene surface promoted by the imidazolium counterions.

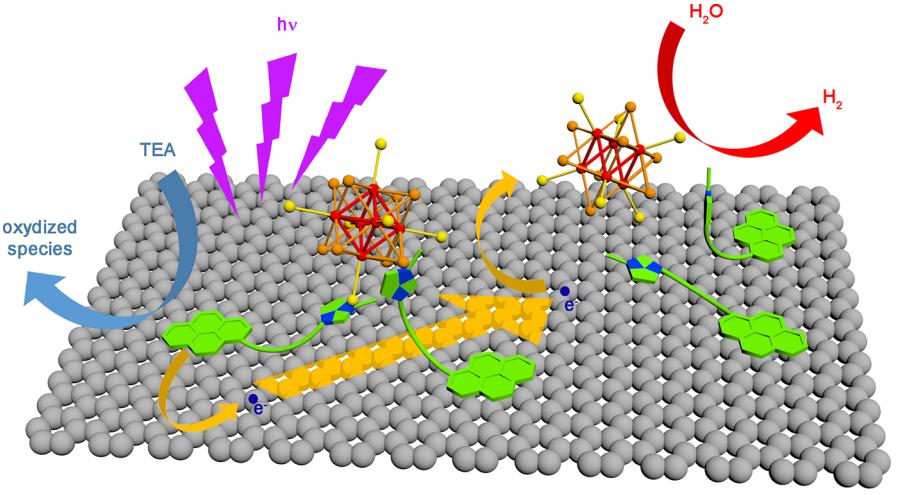

Figure 7. Representation of the photoexcited electron transfer and hydrogen evolution over the **Py_2Mo@Gene** photocatalyst with the assistance of TEA under light irradiation.

DOI: 10.1021/acs.inorgchem.9b02529
Inorg. Chem. XXXX, XXX, XXX−XXX

These results confirm that **Py_2Mo** acts as both the photosensitizer and catalyst for H_2 production under UV−vis irradiation, similar to the $(TBA)_2Mo_6Br^i{}_8F^a{}_6$ photocatalyst. Enhancement of the reaction yields provided by the graphene-supported cluster is due to intimate contact between the **Py_2Mo** catalyst and graphene and to the superior conductivity of graphene because it acts as an efficient electron acceptor and transporter between the immobilized cluster active species (Figure 7). This is in agreement with work reported on the dye-sensitized graphene-based photocatalysts.[59,106]

CONCLUSIONS

We show in this work that red-NIR-emissive octahedral transition-metal clusters can be easily associated to graphene nanosheets using noncovalent interactions. To do so, organic linkers made of an imidazolium head and either a long alkyl chain or a pyrene group were specifically designed to interact with the anionic cluster and graphene surface simultaneously. Adsorption studies demonstrated that the pyrene-containing cation was the most efficient one to bind the anionic cluster on the graphene surface. The components' association was demonstrated by several techniques such as HR-TEM, EDX analyses, and FT-IR and Raman spectroscopies. Photophysical studies of the **Py_2Mo** hybrid complex in solution evidenced a partial ET between the pyrene-containing cations and anionic cluster unit. Taking into account the low amount of pyrene-group triplet state produced during light excitation, we suspect that this ET is more likely to involve the $S_1(Py)$-to-$S_1(Mo)$ transition, followed by an ISC to the $T_1(Mo_6)$ state rather than a transfer from the $T_1(Py)$ to $T_1(Mo_6)$ states.

Once supported on graphene, **Py_2Mo** transfers its energy to the graphene surface, which, in turn, conducts electrons to the catalytic active sites for hydrogen generation. Photocatalytic HER production in water studies has demonstrated the potential of such hybrids in the generation of hydrogen. In fact, the H_2 production efficiency of **Py_2Mo** increases by a factor of 2.8 once grafted onto the graphene surface. Improvement of the H_2 production activity is attributed to the synergetic effect between graphene and the hybrid cluster complex because graphene facilitates the charge-separation activity and enhances ET and electron transfer of the cluster photocatalyst. In addition, the extended aromatic lattice and, as a consequence, the excellent electronic conduction of graphene sheets are preserved during the grafting of **Py_2Mo** thanks to the use of noncovalent interactions to maintain the assembly. Hence, this supramolecular strategy opens up wide perspectives in terms of research prospects to design the most efficient anionic clusters/graphene hybrids for H_2 production.

EXPERIMENTAL SECTION

Reagents and Solvents. Graphite, triethylamine (TEA), diethyl ether, methanol, acetone (ACS analytical grade), dichloromethane (Chromasolv for high-performance liquid chromatography), and anhydrous *N*,*N*-dimethylformamide (DMF) were obtained from commercial resources (Sigma-Aldrich and Scharlau). Graphene nanoplatelet aggregates (surface area 500 m^2/g) were purchased from Strem. The $Cs_2Mo_6I^i{}_8(O_2CC_2F_5)^a{}_6$ (**Cs_2Mo**) precursor was prepared by following reported procedures.[33] The 1-methyl-3-[4-(pyren-1-yl)butyl]-1*H*-imidazol-3-ium bromide (**PyBr**) salt was prepared in a two-step reaction from 2-pyrenebutanol,[107] as described in the literature.[108] Dichloromethane and diethyl ether were dried and deoxygenated by passing these solvents through commercial columns of copper oxide, followed by alumina under nitrogen.

Synthesis of the Materials. *Preparation of the **Py_2Mo** Complex.* To an acetone solution of **Cs_2Mo** was added a solution of **PyBr** in methanol under argon. The mixture was magnetically stirred for 48 h in the dark and then filtered through a Celite pad. The orange solution was then evaporated to yield a red-orange powder. ^1H NMR (400 MHz, acetone-d_6): δ 1.96 (m, 2H, $-CH_2-$), 1.77 (m, 2H, $-CH_2-$), 3.81 (s, 3H, CH_3N), 4.25 (t, 2H, J = 7.1 Hz, $-CH_2N$), 7.67 (t, 1H, J = 1.7 Hz, $-NCHCHN-$), 7.77 (t, 1H, J = 1.7 Hz, $-NCHCHN-$), 8.36−7.95 (m, 9H, C_{Ar}), 9.08 (s, 1H, CH, $-NCHN-$). ^{19}F NMR (376 MHz, acetone-d_6): δ −83 (3F), −120 (2F). ESI-MS (CH_3CN): m/z 1284.3 [M^{2-}], 339.5 [M^+].

*Synthesis of 1-Methyl-3-nonylimidazolium Bromide (**ImBr**).* 1-*N*-Methylimidazole (1.03 g, 12.5 mmol) and 1-bromononane (3.33 g, 15 mmol) were mixed with 50 mL of $CHCl_3$. The mixture was stirred under reflux for 15 h. After evaporation of the solvent under vacuum, the obtained colorless oil was washed three times with 50 mL of a cyclohexane/ethyl actetate mixture (1:1). The oil was recovered via a separation funnel and dried under vacuum to yield the desired compound (yield: 67%). ^1H NMR (400 MHz, acetone-d_6): δ 0.79 (t, 3H, CH_3), 1.25−1.16 (m, 14H, $(CH_2)_7$), 1.84 (m, 2H, $-CH_2CH_2N$), 4.10 (s, 3H, CH_3N), 4.25 (t, 2H, $-CH_2N$), 7.45 (1H, s, $-NCHCHN-$), 7.65 (1H, s, $-NCHCHN-$), 10.24 (1H, s, $-NCHN-$). ESI-MS (CH_3CN): m/z 223.4 [M^+].

*Preparation of the **Im_2Mo** Complex.* To an acetone solution of **Cs_2Mo** was added a solution of **ImBr** in methanol under argon. The mixture was magnetically stirred for 48 h in the dark and then was filtered through a Celite pad. The orange solution was then evaporated to yield a red-orange powder. ^1H NMR (400 MHz, acetone-d_6): δ 0.88 (t, 3H, CH_3), 1.37−1.28 (m, 14H, $(CH_2)_7$), 1.98 (m, 2H, $-CH_2CH_2N$), 4.11 (s, 3H, CH_3N), 4.41 (t, 2H, $-CH_2N$), 7.77 (1H, s, $-NCHCHN-$), 7.83 (1H, s, $-NCHCHN-$), 9.15 (1H, s, $-NCHN-$). ^{19}F NMR (acetone-d_6): δ −83 (3F), −120 (2F). ESI-MS (CH_3CN): m/z 1284.3 [M^{2-}], 223.4 [M^+].

*Preparation of the **Py_2Mo@Gene** Nanocomposite.* An excess of **Py_2Mo** (22 mg, 0.007 mmol) was added to a graphene suspension (15 mg in 60 mL of dried dichloromethane) in a Schlenk flask under argon. The mixture was sonicated with an ultrasound source (400 W, Branson ultrasonic bath) for 1 h and magnetically stirred for 24 h. The solid product was separated from the solution by filtration under vacuum, washed several times with dichloromethane and diethyl ether, and dried under vacuum to provide 25 mg of a black product identified as the **Py_2Mo@Gene** nanocomposite. This material was stored in a desiccator. The amount of molybdenum present in the sample (1.74%, w/w) was determined by inductively coupled proton analysis of the liquid phase after treatment of the solid with aqua regia. This material was characterized by XRD, HR-TEM, EDS/STEM, IR, and Raman techniques.

ASSOCIATED CONTENT

Supporting Information

The Supporting Information is available free of charge on the ACS Publications website at DOI: 10.1021/acs.inorgchem.9b02529.

Characterization techniques, detailed X-ray structural analysis of **Py_2Mo**, ESI-MS spectra, adsorption experiments, HR-TEM micrographs, EDS/STEM analysis of **Py_2Mo@Gene**, photophysics, laser-flash photolysis experiments, calculations of the **Py_2Mo** singlet and triplet excited states, and photocatalyic H_2 production conditions (PDF)

Accession Codes

CCDC 1866933 contains the supplementary crystallographic data for this paper. These data can be obtained free of charge via www.ccdc.cam.ac.uk/data_request/cif, or by emailing data_request@ccdc.cam.ac.uk, or by contacting The Cambridge Crystallographic Data Centre, 12 Union Road, Cambridge CB2 1EZ, UK; fax: +44 1223 336033.

DOI: 10.1021/acs.inorgchem.9b02529
Inorg. Chem. XXXX, XXX, XXX−XXX

AUTHOR INFORMATION

Corresponding Authors

*E-mail: mfeliz@itq.upv.es.

*E-mail: yann.molard@univ-rennes1.fr.

ORCID

Marta Feliz: 0000-0002-4429-0551

Pedro Atienzar: 0000-0002-0356-021X

Pierric Lemoine: 0000-0002-3465-7815

Yann Molard: 0000-0002-6295-0883

Stéphane Cordier: 0000-0003-0707-3774

Author Contributions

The manuscript was written through contributions of all authors. All authors have given approval to the final version of the manuscript.

Funding

The Severo Ochoa Program (SEV-2016-0683), Ministerio de Ciencia, Innovación y Universidades (PGC2018-099744), Consejo Superior de Investigaciones Científicas (I-Link1063), and University of Rennes are tahnked for financial support.

Notes

The authors declare no competing financial interest.

ACKNOWLEDGMENTS

We thank Dr. Marta Puche for her technical assistance with the preparation of dispersed graphene solutions at the ITQ.

REFERENCES

(1) Cotton, F. A. Metal Atom Clusters in Oxide Systems. *Inorg. Chem.* **1964**, *3* (9), 1217−1220.

(2) Maverick, A. W.; Gray, H. B. Luminescence and Redox Photochemistry of the Molybdenum(Ii) Cluster Mo6cl14(2−1). *J. Am. Chem. Soc.* **1981**, *103* (5), 1298−1300.

(3) Nocera, D. G.; Gray, H. B. Electrochemical reduction of molybdenum(II) and tungsten(II) halide cluster ions. Electrogenerated chemiluminescence of tetradecachlorohexamolybdate(2-) ion. *J. Am. Chem. Soc.* **1984**, *106* (3), 824−825.

(4) Larina, T. V.; Ikorskii, V. N.; Vasenin, N. T.; Anufrienko, V. F.; Naumov, N. G.; Ostanina, E. V.; Fedorov, V. E. Electronic state of rhenium complexes with octahedral chalcocyanide cluster anions [Re(6)Q(8)(CN)(6)](3-) (Q = S, Se, Te). EPR and magnetic susceptibility studies. *Russ. J. Coord. Chem.* **2002**, *28* (8), 554−556.

(5) Tulsky, E. G.; Crawford, N. R. M.; Baudron, S. A.; Batail, P.; Long, J. R. Cluster-to-Metal Magnetic Coupling: Synthesis and Characterization of 25-Electron $[Re_{6-n}Os_nSe_8(CN)_6]^{(5-n)-}$ (n = 1, 2) Clusters and $\{Re_{6-n}Os_nSe_8[CNCu(Me_6tren)]_6\}^{9+}$ (n = 0, 1, 2) Assemblies. *J. Am. Chem. Soc.* **2003**, *125* (50), 15543−15553.

(6) Barras, A.; Cordier, S.; Boukherroub, R. Fast photocatalytic degradation of rhodamine B over [Mo6Br8(N3)6]2- cluster units under sun light irradiation. *Appl. Catal. Appl. Catal., B* **2012**, *123*−*124*, 1−8.

(7) Beltran, A.; Mikhailov, M.; Sokolov, M. N.; Perez-Laguna, V.; Rezusta, A.; Revillo, M. J.; Galindo, F. A photobleaching resistant polymer supported hexanuclear molybdenum iodide cluster for photocatalytic oxygenations and photodynamic inactivation of Staphylococcus aureus. *J. Mater. Chem. B* **2016**, *4* (36), 5975−5979.

(8) Buzek, D.; Hynek, J.; Kucerakova, M.; Kirakci, K.; Demel, J.; Lang, K. MoII Cluster Complex-Based Coordination Polymer as an Efficient Heterogeneous Catalyst in the Suzuki-Miyaura Coupling Reaction. *Eur. J. Inorg. Chem.* **2016**, *2016* (28), 4668−4673.

(9) Feliz, M.; Puche, M.; Atienzar, P.; Concepcion, P.; Cordier, S.; Molard, Y. In situ generation of active molybdenum octahedral clusters for photocatalytic hydrogen production from water and their stabilization onto graphene oxide surfaces. *ChemSusChem* **2016**, *9* (15), 1963−1971.

(10) Daigre, G.; Costuas, K.; Tarasenko, M. S.; Ledneva, A. Y.; Naumov, N. G.; Lemoine, P.; Guizouarn, T.; Molard, Y.; Amela-Cortes, M.; Audebrand, N.; Cordier, S. Stabilization of Ni2+ dimers in hexacyano Mo6 cluster-based Prussian blue derivatives: experimental and theoretical investigations of magnetic properties. *Dalton Trans.* **2018**, *47* (4), 1122−1130.

(11) Garreau, A.; Massuyeau, F.; Cordier, S.; Molard, Y.; Gautron, E.; Bertoncini, P.; Faulques, E.; Wery, J.; Humbert, B.; Bulou, A.; Duvail, J.-L. Color Control in Coaxial Two-Luminophore Nanowires. *ACS Nano* **2013**, *7* (4), 2977−2987.

(12) Zhao, Y.; Lunt, R. R. Transparent Luminescent Solar Concentrators for Large-Area Solar Windows Enabled by Massive Stokes-Shift Nanocluster Phosphors. *Adv. Energy Mater.* **2013**, *3* (9), 1143−1148.

(13) Amela-Cortes, M.; Garreau, A.; Cordier, S.; Faulques, E.; Duvail, J.-L.; Molard, Y. Deep red luminescent hybrid copolymer materials with high transition metal cluster content. *J. Mater. Chem. C* **2014**, *2* (8), 1545−1552.

(14) Prevot, M.; Amela-Cortes, M.; Manna, S. K.; Lefort, R.; Cordier, S.; Folliot, H.; Dupont, L.; Molard, Y. Design and Integration in Electro-Optic Devices of Highly Efficient and Robust Red-NIR Phosphorescent Nematic Hybrid Liquid Crystals Containing [Mo6I8-(OCOCnF2n+1)6]2- (n = 1, 2, 3) Nanoclusters. *Adv. Funct. Mater.* **2015**, *25* (31), 4966−4975.

(15) Robin, M.; Kuai, W.; Amela-Cortes, M.; Cordier, S.; Molard, Y.; Mohammed-Brahim, T.; Jacques, E.; Harnois, M. Epoxy Based Ink as Versatile Material for Inkjet-Printed Devices. *ACS Appl. Mater. Interfaces* **2015**, *7* (39), 21975−21984.

(16) Bigeon, J.; Huby, N.; Amela-Cortes, M.; Molard, Y.; Garreau, A.; Cordier, S.; Bêche, B.; Duvail, J. L. Efficient active waveguiding properties of Mo 6 nano-cluster-doped polymer nanotubes. *Nanotechnology* **2016**, *27* (25), 255201.

(17) Robin, M.; Dumait, N.; Amela-Cortes, M.; Roiland, C.; Harnois, M.; Jacques, E.; Folliot, H.; Molard, Y. Direct Integration of Red-NIR Emissive Ceramic-like AnM6Xi8Xa6Metal Cluster Salts in Organic Copolymers Using Supramolecular Interactions. *Chem. - Eur. J.* **2018**, *24* (19), 4825−4829.

(18) Krasilnikova, A. A.; Shestopalov, M. A.; Brylev, K. A.; Kirilova, I. A.; Khripko, O. P.; Zubareva, K. E.; Khripko, Y. I.; Podorognaya, V. T.; Shestopalova, L. V.; Fedorov, V. E.; Mironov, Y. V. Prospects of molybdenum and rhenium octahedral cluster complexes as X-ray contrast agents. *J. Inorg. Biochem.* **2015**, *144*, 13−17.

(19) Kirakci, K.; Kubát, P.; Fejfarová, K.; Martinčík, J.; Nikl, M.; Lang, K. X-ray Inducible Luminescence and Singlet Oxygen Sensitization by an Octahedral Molybdenum Cluster Compound: A New Class of Nanoscintillators. *Inorg. Chem.* **2016**, *55* (2), 803−809.

(20) Solovieva, A. O.; Kirakci, K.; Ivanov, A. A.; Kubat, P.; Pozmogova, T. N.; Miroshnichenko, S. M.; Vorontsova, E. V.; Chechushkov, A. V.; Trifonova, K. E.; Fufaeva, M. S.; Kretov, E. I.; Mironov, Y. V.; Poveshchenko, A. F.; Lang, K.; Shestopalov, M. A. Singlet Oxygen Production and Biological Activity of Hexanuclear Chalcocyanide Rhenium Cluster Complexes [{Re6Q8}(CN)6]4- (Q = S, Se, Te). *Inorg. Chem.* **2017**, *56* (21), 13491−13499.

(21) Brandhonneur, N.; Hatahet, T.; Amela-Cortes, M.; Molard, Y.; Cordier, S.; Dollo, G. Molybdenum cluster loaded PLGA nanoparticles: An innovative theranostic approach for the treatment of ovarian cancer. *Eur. J. Pharm. Biopharm.* **2018**, *125*, 95−105.

(22) Kumar, P.; Kumar, S.; Cordier, S.; Paofai, S.; Boukherroub, R.; Jain, S. L. Photoreduction of CO2 to methanol with hexanuclear molybdenum [Mo6Br14]2− cluster units under visible light irradiation. *RSC Adv.* **2014**, *4* (20), 10420−10423.

(23) Golden, J. H.; Deng, H. B.; Disalvoa, F. J.; Frechet, J. M. J.; Thompson, P. M. Monodisperse Metal-Clusters 10-Angstroms in Diameter in a Polymeric Host - the Monomer-as-Solvent Approach. *Science* **1995**, *268* (5216), 1463−1466.

(24) Jackson, J. A.; Newsham, M. D.; Worsham, C.; Nocera, D. G. Efficient singlet oxygen generation from polymers derivatized with

DOI: 10.1021/acs.inorgchem.9b02529
Inorg. Chem. XXXX, XXX, XXX−XXX

hexanuclear molybdenum clusters. *Chem. Mater.* **1996**, *8* (2), 558−564.
(25) Cordier, S.; Molard, Y.; Brylev, K. A.; Mironov, Y. V.; Grasset, F.; Fabre, B.; Naumov, N. G. Advances in the Engineering of Near Infrared Emitting Liquid Crystals and Copolymers, Extended Porous Frameworks, Theranostic Tools and Molecular Junctions Using Tailored Re6 Cluster Building Blocks. *J. Cluster Sci.* **2015**, *26*, 53−81.
(26) Cordier, S.; Grasset, F.; Molard, Y.; Amela-Cortes, M.; Boukherroub, R.; Ravaine, S.; Mortier, M.; Ohashi, N.; Saito, N.; Haneda, H. Inorganic Molybdenum Octahedral Nanosized Cluster Units, Versatile Functional Building Block for Nanoarchitectonics. *J. Inorg. Organomet. Polym. Mater.* **2015**, *25* (2), 189−204.
(27) Molard, Y. Clustomesogens: Liquid Crystalline Hybrid Nanomaterials Containing Functional Metal Nanoclusters. *Acc. Chem. Res.* **2016**, *49* (8), 1514−1523.
(28) Guy, K.; Ehni, P.; Paofai, S.; Forschner, R.; Roiland, C.; Amela-Cortes, M.; Cordier, S.; Laschat, S.; Molard, Y. Lord of The Crowns: A New Precious in the Kingdom of Clustomesogens. *Angew. Chem., Int. Ed.* **2018**, *57* (36), 11692−11696.
(29) Sokolov, M. N.; Brylev, K. A.; Abramov, P. A.; Gallyamov, M. R.; Novozhilov, I. N.; Kitamura, N.; Mikhaylov, M. A. Complexes of {W6I8}4+ Clusters with Carboxylates: Preparation, Electrochemistry, and Luminescence. *Eur. J. Inorg. Chem.* **2017**, *2017* (35), 4131−4137.
(30) Sokolov, M. N.; Mihailov, M. A.; Peresypkina, E. V.; Brylev, K. A.; Kitamura, N.; Fedin, V. P. Highly luminescent complexes [Mo6 × 8(n-C3F7COO)6]2- (X = Br, I). *Dalton Trans.* **2011**, *40* (24), 6375−6377.
(31) Kirakci, K.; Kubát, P.; Dušek, M.; Fejfarová, K.; Šícha, V.; Mosinger, J.; Lang, K. A Highly Luminescent Hexanuclear Molybdenum Cluster − A Promising Candidate toward Photoactive Materials. *Eur. J. Inorg. Chem.* **2012**, *19*, 3107−3111.
(32) Kirakci, K.; Kubat, P.; Langmaier, J.; Polivka, T.; Fuciman, M.; Fejfarova, K.; Lang, K. A comparative study of the redox and excited state properties of (nBu4N)2[Mo6 × 14] and (nBu4N)2[Mo6 × 8(CF3COO)6] (X = Cl, Br, or I). *Dalton Trans.* **2013**, *42* (19), 7224−7232.
(33) Amela-Cortes, M.; Molard, Y.; Paofai, S.; Desert, A.; Duvail, J.-L.; Naumov, N. G.; Cordier, S. Versatility of the ionic assembling method to design highly luminescent PMMA nanocomposites containing [M6Qi8La6]n- octahedral nano-building blocks. *Dalton Trans.* **2016**, *45* (1), 237−245.
(34) Mikhailov, M. A.; Brylev, K. A.; Abramov, P. A.; Sakuda, E.; Akagi, S.; Ito, A.; Kitamura, N.; Sokolov, M. N. Synthetic Tuning of Redox, Spectroscopic, and Photophysical Properties of {Mo6I8}4+ Core Cluster Complexes by Terminal Carboxylate Ligands. *Inorg. Chem.* **2016**, *55* (17), 8437−8445.
(35) Riehl, L.; Seyboldt, A.; Strobele, M.; Enseling, D.; Justel, T.; Westberg, M.; Ogilby, P. R.; Meyer, H. J. A ligand substituted tungsten iodide cluster: luminescence *vs.* singlet oxygen production. *Dalton Trans.* **2016**, *45* (39), 15500−15506.
(36) Akagi, S.; Fujii, S.; Horiguchi, T.; Kitamura, N. pK a(L) Dependences of Structural, Electrochemical, and Photophysical Properties of Octahedral Hexamolybdenum(II) Clusters: [Mo6 × 8 L 6]2− (X = Br or I; L = carboxylate). *J. Cluster Sci.* **2017**, *28* (2), 757−772.
(37) Kirakci, K.; Zelenka, J.; Rumlova, M.; Martincik, J.; Nikl, M.; Ruml, T.; Lang, K. Octahedral molybdenum clusters as radio-sensitizers for X-ray induced photodynamic therapy. *J. Mater. Chem. B* **2018**, *6* (26), 4301−4307.
(38) Amela-Cortes, M.; Paofai, S.; Cordier, S.; Folliot, H.; Molard, Y. Tuned Red NIR phosphorescence of polyurethane hybrid composites embedding metallic nanoclusters for oxygen sensing. *Chem. Commun.* **2015**, *51*, 8177−8180.
(39) Kudo, A.; Miseki, Y. Heterogeneous photocatalyst materials for water splitting. *Chem. Soc. Rev.* **2009**, *38* (1), 253−278.
(40) Walter, M. G.; Warren, E. L.; McKone, J. R.; Boettcher, S. W.; Mi, Q.; Santori, E. A.; Lewis, N. S. Solar Water Splitting Cells. *Chem. Rev.* **2010**, *110* (11), 6446−6473.
(41) Maeda, K. Photocatalytic water splitting using semiconductor particles: History and recent developments. *J. Photochem. Photobiol., C* **2011**, *12* (4), 237−268.
(42) Zou, X.; Zhang, Y. Noble metal-free hydrogen evolution catalysts for water splitting. *Chem. Soc. Rev.* **2015**, *44* (15), 5148−5180.
(43) Watanabe, M. Dye-sensitized photocatalyst for effective water splitting catalyst. *Sci. Technol. Adv. Mater.* **2017**, *18* (1), 705−723.
(44) Zheng, D.; Pang, X.; Wang, M.; He, Y.; Lin, C.; Lin, Z. Unconventional Route to Hairy Plasmonic/Semiconductor Core/Shell Nanoparticles with Precisely Controlled Dimensions and Their Use in Solar Energy Conversion. *Chem. Mater.* **2015**, *27* (15), 5271−5278.
(45) Wang, M.; Pang, X.; Zheng, D.; He, Y.; Sun, L.; Lin, C.; Lin, Z. Nonepitaxial growth of uniform and precisely size-tunable core/shell nanoparticles and their enhanced plasmon-driven photocatalysis. *J. Mater. Chem. A* **2016**, *4* (19), 7190−7199.
(46) Wang, M.; Ye, M.; Iocozzia, J.; Lin, C.; Lin, Z. Plasmon-Mediated Solar Energy Conversion via Photocatalysis in Noble Metal/Semiconductor Composites. *Adv. Science* **2016**, *3* (6), 1600024.
(47) Yang, J.; Fu, H.; Yang, D.; Gao, W.; Cong, R.; Yang, T. ZnGa2−xInxS4 ($0 \leq x \leq 0.4$) and Zn1−2y(CuGa)yGa1.7In0.3S4 ($0.1 \leq y \leq 0.2$): Optimize Visible Light Photocatalytic H2 Evolution by Fine Modulation of Band Structures. *Inorg. Chem.* **2015**, *54* (5), 2467−2473.
(48) Yu, W.; Zhang, S.; Chen, J.; Xia, P.; Richter, M. H.; Chen, L.; Xu, W.; Jin, J.; Chen, S.; Peng, T. Biomimetic Z-scheme photocatalyst with a tandem solid-state electron flow catalyzing H2 evolution. *J. Mater. Chem. A* **2018**, *6* (32), 15668−15674.
(49) Hao, Q.; Song, Y.; Ji, H.; Mo, Z.; She, X.; Deng, J.; Muhmood, T.; Wu, X.; Yuan, S.; Xu, H.; Li, H. Surface N modified 2D g-C3N4 nanosheets derived from DMF for photocatalytic H2 evolution. *Appl. Surf. Sci.* **2018**, *459*, 845−852.
(50) Xia, Y.; Cheng, B.; Fan, J.; Yu, J.; Liu, G. Unraveling Photoexcited Charge Transfer Pathway and Process of CdS/Graphene Nanoribbon Composites toward Visible-Light Photocatalytic Hydrogen Evolution. *Small* **2019**, *15* (34), 1902459.
(51) Chang, C.-J.; Lin, Y.-G.; Weng, H.-T.; Wei, Y.-H. Photocatalytic hydrogen production from glycerol solution at room temperature by ZnO-ZnS/graphene photocatalysts. *Appl. Surf. Sci.* **2018**, *451*, 198−206.
(52) Xu, D.; Li, L.; He, R.; Qi, L.; Zhang, L.; Cheng, B. Noble metal-free RGO/TiO2 composite nanofiber with enhanced photocatalytic H2-production performance. *Appl. Surf. Sci.* **2018**, *434*, 620−625.
(53) Osterloh, F. E. Inorganic Materials as Catalysts for Photochemical Splitting of Water. *Chem. Mater.* **2008**, *20* (1), 35−54.
(54) Sun, Y.; Wu, Q.; Shi, G. Graphene based new energy materials. *Energy Environ. Sci.* **2011**, *4* (4), 1113−1132.
(55) Wang, J.; Cui, W.; Liu, Q.; Xing, Z.; Asiri, A. M.; Sun, X. Recent Progress in Cobalt-Based Heterogeneous Catalysts for Electrochemical Water Splitting. *Adv. Mater.* **2016**, *28* (2), 215−230.
(56) Kamat, P. V. Graphene-Based Nanoassemblies for Energy Conversion. *J. Phys. Chem. Lett.* **2011**, *2* (3), 242−251.
(57) Han, L.; Wang, P.; Dong, S. Progress in graphene-based photoactive nanocomposites as a promising class of photocatalyst. *Nanoscale* **2012**, *4* (19), 5814−5825.
(58) Xiang, Q.; Yu, J. Graphene-Based Photocatalysts for Hydrogen Generation. *J. Phys. Chem. Lett.* **2013**, *4* (5), 753−759.
(59) Huo, J.; Zhang, Y.-B.; Zou, W.-Y.; Hu, X.; Deng, Q.; Chen, D. Mini-review on an engineering approach towards the selection of transition metal complex-based catalysts for photocatalytic H2 production. *Catal. Sci. Technol.* **2019**, *9* (11), 2716−2727.
(60) Attia, Y.; Samer, M. Metal clusters: New era of hydrogen production. *Renewable Sustainable Energy Rev.* **2017**, *79*, 878−892.
(61) Peiris, S.; McMurtrie, J.; Zhu, H.-Y. Metal nanoparticle photocatalysts: emerging processes for green organic synthesis. *Catal. Sci. Technol.* **2016**, *6* (2), 320−338.

DOI: 10.1021/acs.inorgchem.9b02529
Inorg. Chem. XXXX, XXX, XXX−XXX

(62) Kim, H.-i.; Moon, G.-h.; Monllor-Satoca, D.; Park, Y.; Choi, W. Solar Photoconversion Using Graphene/TiO2 Composites: Nano-graphene Shell on TiO2 Core versus TiO2 Nanoparticles on Graphene Sheet. *J. Phys. Chem. C* **2012**, *116* (1), 1535−1543.
(63) Chang, K.; Mei, Z.; Wang, T.; Kang, Q.; Ouyang, S.; Ye, J. MoS2/Graphene Cocatalyst for Efficient Photocatalytic H2 Evolution under Visible Light Irradiation. *ACS Nano* **2014**, *8* (7), 7078−7087.
(64) Li, H.; Yu, K.; Li, C.; Tang, Z.; Guo, B.; Lei, X.; Fu, H.; Zhu, Z. Charge-Transfer Induced High Efficient Hydrogen Evolution of MoS2/graphene Cocatalyst. *Sci. Rep.* **2015**, *5*, 18730.
(65) Georgakilas, V.; Tiwari, J. N.; Kemp, K. C.; Perman, J. A.; Bourlinos, A. B.; Kim, K. S.; Zboril, R. Noncovalent Functionalization of Graphene and Graphene Oxide for Energy Materials, Biosensing, Catalytic, and Biomedical Applications. *Chem. Rev.* **2016**, *116* (9), 5464−5519.
(66) Li, X.; Yu, J.; Wageh, S.; Al-Ghamdi, A. A.; Xie, J. Graphene in Photocatalysis: A Review. *Small* **2016**, *12* (48), 6640−6696.
(67) Fabre, B.; Cordier, S.; Molard, Y.; Perrin, C.; Ababou-Girard, S.; Godet, C. Electrochemical and Charge Transport Behavior of Molybdenum-Based Metallic Cluster Layers Immobilized on Modified n- and p-Type Si(111) Surfaces. *J. Phys. Chem. C* **2009**, *113* (40), 17437−17446.
(68) Godet, C.; Ababou-Girard, S.; Fabre, B.; Molard, Y.; Fadjie-Djomkam, A. B.; Deputier, S.; Guilloux-Viry, M.; Cordier, S. Surface immobilization of Mo6I8 octahedral cluster cores on functionalized amorphous carbon using a pyridine complexation strategy. *Diamond Relat. Mater.* **2015**, *55*, 131−138.
(69) Cordier, S.; Fabre, B.; Molard, Y.; Fadjie-Djomkam, A.-B.; Turban, P.; Tricot, S.; Ababou-Girard, S.; Godet, C. Elaboration, Characterizations, and Energetics of Robust Mo6 Cluster-Terminated Silicon-Bound Molecular Junctions. *J. Phys. Chem. C* **2016**, *120* (4), 2324−2334.
(70) Wang, H.; Ma, K.; Xu, B.; Tian, W. Tunable Supramolecular Interactions of Aggregation-Induced Emission Probe and Graphene Oxide with Biomolecules: An Approach toward Ultrasensitive Label-Free and "Turn-On" DNA Sensing. *Small* **2016**, *12* (47), 6613−6622.
(71) Sabater, S.; Mata, J. A.; Peris, E. Immobilization of Pyrene-Tagged Palladium and Ruthenium Complexes onto Reduced Graphene Oxide: An Efficient and Highly Recyclable Catalyst for Hydrodefluorination. *Organometallics* **2015**, *34* (7), 1186−1190.
(72) Zhang, X.; Huisman, E. H.; Gurram, M.; Browne, W. R.; van Wees, B. J.; Feringa, B. L. Supramolecular Chemistry on Graphene Field-Effect Transistors. *Small* **2014**, *10* (9), 1735−1740.
(73) Zhou, X.; Wu, T.; Ding, K.; Hu, B.; Hou, M.; Han, B. Dispersion of graphene sheets in ionic liquid [bmim][PF6] stabilized by an ionic liquid polymer. *Chem. Commun.* **2010**, *46* (3), 386−388.
(74) Wang, J.; Chen, Z.; Chen, B. Adsorption of Polycyclic Aromatic Hydrocarbons by Graphene and Graphene Oxide Nanosheets. *Environ. Sci. Technol.* **2014**, *48* (9), 4817−4825.
(75) Shakourian-Fard, M.; Jamshidi, Z.; Bayat, A.; Kamath, G. Meta-Hybrid Density Functional Theory Study of Adsorption of Imidazolium- and Ammonium-Based Ionic Liquids on Graphene Sheet. *J. Phys. Chem. C* **2015**, *119* (13), 7095−7108.
(76) Srinivasan, S.; Shin, W. H.; Choi, J. W.; Coskun, A. A bifunctional approach for the preparation of graphene and ionic liquid-based hybrid gels. *J. Mater. Chem. A* **2013**, *1* (1), 43−48.
(77) Kirakci, K.; Fejfarova, K.; Kucerakova, M.; Lang, K. Hexamolybdenum Cluster Complexes with Pyrene and Anthracene Carboxylates: Ultrabright Red Emitters with the Antenna Effect. *Eur. J. Inorg. Chem.* **2014**, *14*, 2331−2336.
(78) Preetz, W.; Bublitz, D.; Von Schnering, H. G.; Saßmannshausen, J. Darstellung, Kristallstruktur und spektroskopische Eigenschaften der Clusteranionen [(Mo6Br 8i)X 6a]2− mit Xa = F, Cl, Br, I. *Z. Anorg. Allg. Chem.* **1994**, *620* (2), 234−246.
(79) Schoonover, J. R.; Zietlow, T. C.; Clark, D. L.; Heppert, J. A.; Chisholm, M. H.; Gray, H. B.; Sattelberger, A. P.; Woodruff, W. H. Resonance Raman Spectra of [M6 × 8Y6]2- Cluster Complexes (M = Mo, W; X, Y = Cl, Br, I). *Inorg. Chem.* **1996**, *35* (22), 6606−6613.
(80) Ferrari, A. C. Raman spectroscopy of graphene and graphite: Disorder, electron−phonon coupling, doping and nonadiabatic effects. *Solid State Commun.* **2007**, *143* (1), 47−57.
(81) Asher, S. A. Ultraviolet resonance Raman spectrometry for detection and speciation of trace polycyclic aromatic hydrocarbons. *Anal. Chem.* **1984**, *56* (4), 720−724.
(82) Rumelfanger, R.; Asher, S. A.; Perry, M. B. UV Resonance Raman Characterization of Polycyclic Aromatic Hydrocarbons in Coal Liquid Distillates. *Appl. Spectrosc.* **1988**, *42* (2), 267−272.
(83) Larsen, J.; Puntoriero, F.; Pascher, T.; McClenaghan, N.; Campagna, S.; Åkesson, E.; Sundström, V. Extending the Light-Harvesting Properties of Transition-Metal Dendrimers. *ChemPhysChem* **2007**, *8* (18), 2643−2651.
(84) Amelia, M.; Lavie-Cambot, A.; McClenaghan, N. D.; Credi, A. A ratiometric luminescent oxygen sensor based on a chemically functionalized quantum dot. *Chem. Commun.* **2011**, *47* (1), 325−327.
(85) Ramirez-Tagle, R.; Arratia-Pérez, R. Electronic structure and molecular properties of the [Mo6 × 8L6]2−; X = Cl, Br, I; L = F, Cl, Br, I clusters. *Chem. Phys. Lett.* **2008**, *460* (4−6), 438−441.
(86) Costuas, K.; Garreau, A.; Bulou, A.; Fontaine, B.; Cuny, J.; Gautier, R.; Mortier, M.; Molard, Y.; Duvail, J. L.; Faulques, E.; Cordier, S. Combined theoretical and time-resolved photoluminescence investigations of [Mo6Bri8Bra6]2- metal cluster units: evidence of dual emission. *Phys. Chem. Chem. Phys.* **2015**, *17* (43), 28574−28585.
(87) Karpovich, D. S.; Blanchard, G. J. Relating the polarity-dependent fluorescence response of pyrene to vibronic coupling. Achieving a fundamental understanding of the py polarity scale. *J. Phys. Chem.* **1995**, *99* (12), 3951−3958.
(88) Camerel, F.; Kinloch, F.; Jeannin, o.; Robin, M.; nayak, s. K.; Jacques, E.; Brylev, K.; Naumov, N. G.; Molard, Y. Ionic Columnar Clustomesogens: Associations between Anionic Hexanuclear Rhenium Clusters and Liquid Crystalline Triphenylene Tethered Imidazoliums. *Dalton Trans.* **2018**, *47*, 10884−10896.
(89) Vining, W. J.; Caspar, J. V.; Meyer, T. J. The influence of environmental effects on excited-state lifetimes. The effect of ion pairing on metal-to-ligand charge transfer excited states. *J. Phys. Chem.* **1985**, *89* (7), 1095−1099.
(90) Divya, K. P.; Savithri, S.; Ajayaghosh, A. A fluorescent molecular probe for the identification of zinc and cadmium salts by excited state charge transfer modulation. *Chem. Commun.* **2014**, *50* (45), 6020−6022.
(91) Ma, Y.; Liu, S.; Yang, H.; Zeng, Y.; She, P.; Zhu, N.; Ho, C.-L.; Zhao, Q.; Huang, W.; Wong, W.-Y. Luminescence Color Tuning by Regulating Electrostatic Interaction in Light-Emitting Devices and Two-Photon Excited Information Decryption. *Inorg. Chem.* **2017**, *56* (5), 2409−2416.
(92) Ma, Y.; She, P.; Zhang, K. Y.; Yang, H.; Qin, Y.; Xu, Z.; Liu, S.; Zhao, Q.; Huang, W. Dynamic metal-ligand coordination for multicolour and water-jet rewritable paper. *Nat. Commun.* **2018**, *9* (1), 3.
(93) Pankasem, S.; Thomas, J. K. Reflectance spectroscopic studies of the cation radical and the triplet of pyrene on alumina. *J. Phys. Chem.* **1991**, *95* (18), 6990−6996.
(94) Pina, J.; Pinheiro, D.; Nascimento, B.; Pineiro, M.; Seixas de Melo, J. S. The effect of polyaromatic hydrocarbons on the spectral and photophysical properties of diaryl-pyrrole derivatives: an experimental and theoretical study. *Phys. Chem. Chem. Phys.* **2014**, *16* (34), 18319−18326.
(95) Takahashi, T.; Shizu, K.; Yasuda, T.; Togashi, K.; Adachi, C. Donor−acceptor-structured 1,4-diazatriphenylene derivatives exhibiting thermally activated delayed fluorescence: design and synthesis, photophysical properties and OLED characteristics. *Sci. Technol. Adv. Mater.* **2014**, *15*, 034202.
(96) Kurata, R.; Tanaka, K.; Ito, A. Isolation and Characterization of Persistent Radical Cation and Dication of 2,7-Bis(dianisylamino)-pyrene. *J. Org. Chem.* **2016**, *81* (1), 137−145.

DOI: 10.1021/acs.inorgchem.9b02529
Inorg. Chem. XXXX, XXX, XXX−XXX

(97) Cao, L.; Meziani, M. J.; Sahu, S.; Sun, Y.-P. Photoluminescence Properties of Graphene versus Other Carbon Nanomaterials. *Acc. Chem. Res.* **2013**, *46* (1), 171−180.
(98) Economopoulos, S. P.; Tagmatarchis, N. Multichromophores Onto Graphene: Supramolecular Non-Covalent Approaches for Efficient Light Harvesting. *J. Phys. Chem. C* **2015**, *119* (15), 8046−8053.
(99) de Miguel, M.; Álvaro, M.; García, H. Graphene as a Quencher of Electronic Excited States of Photochemical Probes. *Langmuir* **2012**, *28* (5), 2849−2857.
(100) Atienzar, P.; Primo, A.; Lavorato, C.; Molinari, R.; García, H. Preparation of Graphene Quantum Dots from Pyrolyzed Alginate. *Langmuir* **2013**, *29* (20), 6141−6146.
(101) Min, S.; Lu, G. Sites for High Efficient Photocatalytic Hydrogen Evolution on a Limited-Layered MoS2 Cocatalyst Confined on Graphene Sheets—The Role of Graphene. *J. Phys. Chem. C* **2012**, *116* (48), 25415−25424.
(102) Liu, M.; Li, F.; Sun, Z.; Ma, L.; Xu, L.; Wang, Y. Noble-metal-free photocatalysts MoS2-graphene/CdS mixed nanoparticles/nanorods morphology with high visible light efficiency for H2 evolution. *Chem. Commun.* **2014**, *50* (75), 11004−11007.
(103) Latorre-Sánchez, M.; Esteve-Adell, I.; Primo, A.; García, H. Innovative preparation of MoS2−graphene heterostructures based on alginate containing (NH4)2MoS4 and their photocatalytic activity for H2 generation. *Carbon* **2015**, *81*, 587−596.
(104) Meng, F.; Li, J.; Cushing, S. K.; Zhi, M.; Wu, N. Solar Hydrogen Generation by Nanoscale p−n Junction of p-type Molybdenum Disulfide/n-type Nitrogen-Doped Reduced Graphene Oxide. *J. Am. Chem. Soc.* **2013**, *135* (28), 10286−10289.
(105) Matsumoto, Y.; Koinuma, M.; Ida, S.; Hayami, S.; Taniguchi, T.; Hatakeyama, K.; Tateishi, H.; Watanabe, Y.; Amano, S. Photoreaction of Graphene Oxide Nanosheets in Water. *J. Phys. Chem. C* **2011**, *115* (39), 19280−19286.
(106) Xie, G.; Zhang, K.; Guo, B.; Liu, Q.; Fang, L.; Gong, J. R. Graphene-Based Materials for Hydrogen Generation from Light-Driven Water Splitting. *Adv. Mater.* **2013**, *25* (28), 3820−3839.
(107) Furuta, K.; Tomokiyo, K.; Kuo, M. T.; Ishikawa, T.; Suzuki, M. Molecular design of glutathione-derived biochemical probes targeting the GS-X pump. *Tetrahedron* **1999**, *55* (24), 7529−7540.
(108) Wittmann, S.; Schätz, A.; Grass, R. N.; Stark, W. J.; Reiser, O. A Recyclable Nanoparticle-Supported Palladium Catalyst for the Hydroxycarbonylation of Aryl Halides in Water. *Angew. Chem., Int. Ed.* **2010**, *49* (10), 1867−1870.

DOI: 10.1021/acs.inorgchem.9b02529
Inorg. Chem. XXXX, XXX, XXX−XXX